Sensitive control of broad-area semiconductor lasers by cavity shape

Cite as: APL Photon. 7, 056106 (2022); doi: 10.1063/5.0087048
Submitted: 31 January 2022 • Accepted: 2 May 2022 •
Published Online: 23 May 2022

Kyungduk Kim,[1] Stefan Bittner,[2] Yuhao Jin,[3] Yongquan Zeng,[3] Stefano Guazzotti,[4] Ortwin Hess,[4] Qi Jie Wang,[3] and Hui Cao[1,a)]

AFFILIATIONS

[1] Department of Applied Physics, Yale University, New Haven, Connecticut 06520, USA
[2] Chair in Photonics, LMOPS EA-4423 Laboratory, CentraleSupélec and Université de Lorraine, Metz 57070, France
[3] Center for OptoElectronics and Biophotonics, School of Electrical and Electronic Engineering, School of Physical and Mathematical Science, and Photonics Institute, Nanyang Technological University, 639798, Singapore
[4] School of Physics and CRANN Institute, Trinity College Dublin, Dublin 2, Ireland

[a)] **Author to whom correspondence should be addressed:** hui.cao@yale.edu

ABSTRACT

The ray dynamics of optical cavities exhibits bifurcation points: special geometries at which ray trajectories switch abruptly between stable and unstable. A prominent example is the Fabry–Perot cavity with two planar mirrors, which is widely employed for broad-area semiconductor lasers. Such cavities support lasing in a relatively small number of transverse modes, and the laser is highly susceptible to filamentation and irregular pulsations. Here, we demonstrate experimentally that a slight deviation from this bifurcation point (planar cavity) dramatically changes the laser performance. In a near-planar cavity with two concave mirrors, the number of transverse lasing modes increases drastically. While the spatial coherence of the laser emission is reduced, the divergence angle of the output beam remains relatively narrow. Moreover, the spatiotemporal lasing dynamics becomes significantly more stable compared to that in a Fabry–Perot cavity. Our near-planar broad-area semiconductor laser has higher brightness, better directionality, and hence allows shorter integration times than an incandescent lamp while featuring sufficiently low speckle contrast at the same time, making it a vastly superior light source for speckle-free imaging. Furthermore, our method of controlling spatiotemporal dynamics with extreme sensitivity near a bifurcation point may be applied to other types of high-power lasers and nonlinear dynamic systems.

I. INTRODUCTION

The cavity is a crucial component determining the performance of a laser. There has been much effort in tailoring the cavity geometry to control lasing dynamics.[1] Traditional cavity design is based on ray optics that tracks the propagation of optical rays inside a cavity. Due to the principle of ray-wave correspondence, the ray dynamics allows us to predict many properties of the actual cavity resonances, such as their spatial structures and output patterns. Most solid state and gas laser cavities have two concave mirrors arranged in such a way that the axial orbit is stable.[2–4] In contrast, Fabry–Perot cavities with two planar facets have been widely adopted for semiconductor edge-emitting lasers. However, planar broad-area high-power semiconductor lasers are highly susceptible to filamentation and irregular pulsation due to strong nonlinear interactions of the optical field and the gain medium.[5–11]

An interesting aspect of the planar Fabry–Perot cavity [see Fig. 1(b)] with a profound impact on the lasing dynamics is that it is situated at the bifurcation between stable cavities with concave mirrors [Fig. 1(c)] and unstable cavities with convex mirrors. One way of suppressing the semiconductor laser instabilities is to destabilize the cavity ray dynamics by tilting the planar facet[12,13] or changing it to a convex shape.[14–17] Such cavities lase only in the fundamental mode, which stabilizes the temporal dynamics.[18] However, at high pump powers, additional transverse modes can lase, nonetheless, and their nonlinear interactions with the gain medium bring back filaments and pulsations.

Instead of considering unstable cavities, we have moved deeply into the regime of stable cavities for highly multimode lasing in previous studies.[19] By replacing the flat mirrors with concave ones of large curvature, high-order transverse modes are well confined in near-concentric cavities.[20,21] Their small transverse

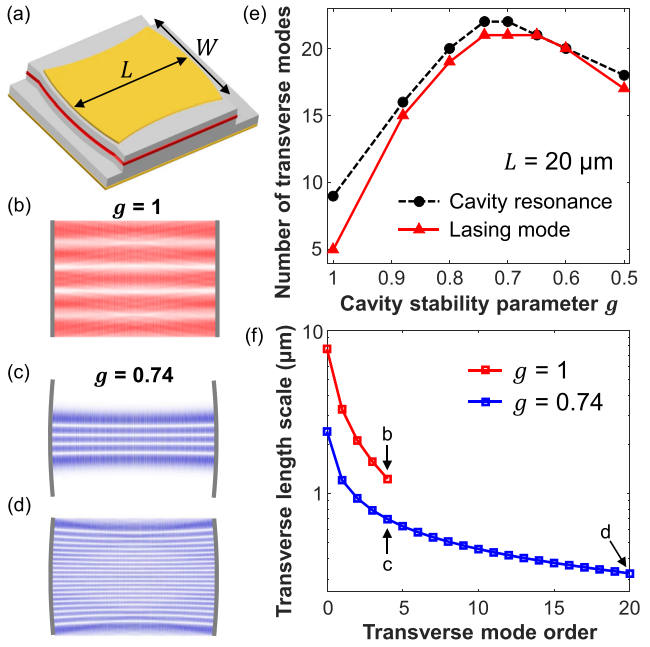

FIG. 1. Optical modes in a near-planar laser cavity. (a) Schematic of a near-planar broad-area semiconductor laser with cavity length L and width W. (b) A passive mode of a planar cavity ($g = 1$) without mirror curvature, exhibiting a spatial profile extended over the entire facet. (c) A passive mode of the same transverse order in a near-planar cavity ($g = 0.74$), showing enhanced lateral confinement. (d) The profile of the highest-order transverse mode confined in the near-planar cavity ($g = 0.74$), featuring greatly decreased transverse wavelength. (e) The number of transverse modes in near-planar cavities. Black dashed curve: passive resonances with a quality factor higher than $0.8Q_{max}$. Red solid curve: lasing modes at two times the lasing threshold in the presence of gain competition. (f) Reduction of the transverse characteristic length scale of the passive modes (on a logarithmic scale). Each curve stops at the highest-order transverse lasing mode calculated in (e). The modes in (b)–(d) are indicated with arrows.

wavelength prevents filament formation and mitigates spatiotemporal instabilities.[19,21] In contrast, such stable cavities confine ray trajectories with a large range of propagation directions, leading to strongly divergent far-field emission.[21] For efficient collection of the laser emission, it is desirable to also attain high output directionality by staying closer to the Fabry–Perot geometry while maintaining low spatial coherence and stable lasing dynamics.

Here, we investigate broad-area edge-emitting semiconductor laser performance as a function of the resonator geometry in the vicinity of the bifurcation at the planar cavity geometry. We experimentally demonstrate that a tiny modification of the Fabry–Perot cavity has a profound impact on the lasing dynamics and spatial coherence. As we slightly curve the two end facets to form a near-planar stable cavity with concave mirrors, the spatial structures of cavity resonances are strongly modified, which in turn alters their nonlinear interactions with the gain medium (GaAs quantum well). Consequently, the spatiotemporal stability of the lasing dynamics in near-planar cavities is greatly improved. Such a simple scheme of mitigating instabilities will facilitate the stabilization of high-power broad-area semiconductor lasers for applications in material processing[22] and laser pumping,[23] as well as biomedical applications.[24]

Moreover, the number of transverse lasing modes drastically increases compared to that in the planar Fabry–Perot cavity, resulting in a sharp drop in the spatial coherence of the emission. At the same time, the output beam has a far-field divergence angle notably smaller than that of stable cavities with strongly curved facets.[21] This combination of sufficiently low spatial coherence and relatively good emission directionality makes our laser an ideal illumination source for speckle-free full-field imaging.[25,26]

II. NEAR-PLANAR CAVITY

A. Ray dynamics

Starting with the Fabry–Perot cavity, we gradually change the planar mirrors to concave ones, while keeping the distance L between the mirrors and the cavity width W constant. The cavity stability parameter is given by $g = 1 - L/R$, where R is the radius of curvature of the end mirrors. In a Fabry–Perot cavity with $g = 1$, an optical ray is trapped only if it propagates parallel to the cavity axis (perpendicular to the end mirrors). When the propagation direction of a ray deviates from the cavity axis, it runs laterally out of the cavity after a few round trips (see the supplementary material).

With concave mirrors at both ends, g becomes less than 1, and the ray dynamics changes substantially. In a near-planar cavity with even slightly curved mirrors [Fig. 1(a)], the axial orbit becomes stable, and additional trajectories propagating with a slight angle with respect to the cavity axis remain confined laterally.

B. Cavity resonances

The dramatic change in the ray dynamics from planar to near-planar cavities has a strong influence on the spatial structure of the cavity resonances (i.e., solutions of the wave equation of the passive cavity). Due to the lack of lateral confinement in a Fabry–Perot cavity, the cavity resonances extend laterally across the entire end facets [Fig. 1(b)]. As the higher-order transverse modes exhibit larger transverse wavevector components $k_\perp$, their lateral leakage is stronger, and their quality (Q) factor is lower. In contrast, the lateral confinement of rays by concave mirrors reduces the transverse width of the cavity resonance, as shown in Fig. 1(c). The existence of confined trajectories in the vicinity of the cavity axis greatly enhances the Q factor of high-order transverse modes. Therefore, even a near-planar cavity can feature a relatively large number of transverse modes [Fig. 1(e)].

The existence of high-order transverse modes and their lateral confinement in a stable cavity lead to a sharp drop in the characteristic length scale ξ of the optical intensity variation in the transverse direction. This has a profound impact on the nonlinear interactions between the cavity modes and the gain medium.[19,27] ξ is given by the full-width at half-maximum of the transverse intensity correlation function. Since ξ varies in the longitudinal direction for $g \neq 1$, we average its value along the cavity axis. Higher-order transverse modes have smaller ξ. In a Fabry–Perot cavity with a GaAs quantum well (gain medium), only low-order transverse modes are confined, and intensity variations on the scale $\xi \gg \lambda$ result in local carrier-induced refractive index changes due to spatial hole burning. Optical lensing and self-focusing effects lead to the formation of

spatial filaments, which are inherently unstable and cause irregular pulsations.

In a stable cavity, the ξ of high-order transverse modes can be sufficiently small, so local refractive index variations cannot focus light and create a filament. In addition, the spatial modulation of the refractive index on such short scales supersedes and disrupts the large lenses induced by lower-order transverse modes, thus preventing filamentation. Therefore, an efficient way of reducing the spatiotemporal instability in a broad-area semiconductor quantum well laser is to minimize ξ via a stable cavity.[19]

C. High-Q modes

To maintain a relatively narrow angular spread of the far-field emission, we optimize the stable cavity geometry in the vicinity of the planar cavity. In particular, we maximize the number of transverse lasing modes within the range $0.5 \leq g \leq 1$. Since the lasing modes need to have high Q factors, we calculate the high-Q transverse modes of passive cavities. Because the GaAs quantum well has preferential gain for transverse electric (TE) polarization, we calculate the modes with the electric field in the plane of incidence (p-polarization). The simulated cavities have the same aspect ratio $L/W = \sqrt{2}$ as the experimental ones, but are $L = 20$ μm long. The refractive index $n = 3.37$ in the cavity is equal to the effective index of the fundamental TE mode guided in the vertical direction of a GaAs/AlGaAs epiwafer. The wavelength range of numerical simulations is centered around 800 nm, which matches the gain spectrum of the GaAs quantum well.

The fundamental transverse mode has the highest quality factor Q_{max}, which determines the lasing threshold. Q_{max} depends on the cavity length L and mirror reflectivity. It barely changes with g, and thus, curving the end facets has little effect on the lasing threshold. However, the Q factors of the high-order transverse modes are greatly improved in a stable cavity with concave mirrors, leading to a drastic increase in the number of lasing modes.

We show the number M_h of transverse modes with $Q > 0.8Q_{max}$ in Fig. 1(e). As g decreases from 1, M_h increases rapidly and reaches its maximum at $g = 0.7$, and then decreases. While the sharp rise results from the better lateral confinement of high-order transverse modes, the subsequent drop in M_h is caused by the reduced reflectivity for rays with non-perpendicular incidence (see the supplementary material). With increasing mirror curvature, the angles of incidence θ_i at the semiconductor–air interface increase, and for TE polarization, the reflectivity decreases for θ_i going from 0 toward the Brewster angle.[21] Therefore, the number of high-Q transverse modes is maximal for a near-planar cavity.

D. Number of lasing modes

Due to their competition for gain, not all high-Q modes will lase eventually. Taking into account the spatial overlap of these modes, we compute the number M_l of transverse lasing modes using the Single-Pole-Approximation Steady-state *Ab initio* Lasing Theory (SPA-SALT).[28] Figure 1(e) compares M_l at two times the lasing threshold to M_h. The difference between M_h and M_l reflects the strength of modal competition for gain. In the Fabry–Perot cavity of $g = 1$, only five transverse modes manage to lase among nine high-Q passive modes. In contrast, 21 out of 22 high-Q transverse modes lase in a near-planar cavity of $g = 0.7$. Thus, slightly curving the end mirrors raises the number of transverse lasing modes by a factor of 4.

The transverse length scale ξ of the intensity variation is plotted for every transverse lasing mode in Fig. 1(f). For the same transverse mode order, ξ is much smaller for $g = 0.74$ than for $g = 1$ due to better lateral confinement. In addition, more higher-order transverse modes lase, further reducing ξ. The shortest ξ, corresponding to the highest-order transverse lasing mode, drops four times from $g = 1$ to 0.74. The dramatic decrease in the transverse intensity variation length scale prevents the formation of carrier-induced optical lenses. It suppresses self-focusing that would lead to filamentation and instabilities. As a result, the near-planar cavity features the improved laser stability, similar to a cavity with chaotic ray dynamics.[27]

III. HIGHLY MULTIMODE LASING

We fabricate near-planar laser cavities on a GaAs quantum well epiwafer. The cavity structure is defined by dry etching with an etch depth of 3.5 μm (see the supplementary material). While the radius of curvature R of the two end facets is varied from device to device, the longitudinal cavity length $L = 400$ μm and transverse cavity width $W = 283$ μm are kept constant. The aspect ratio $L/W = \sqrt{2}$ is consistent with the simulations in Fig. 1, even though the cavity size is 20 times larger. To reduce sample heating, we operate the lasers at room temperature with a pulse duration of 2 μs and a repetition rate lower than 1 Hz. All devices with different g have similar lasing thresholds of ~0.5 A, corresponding to a current density of 0.5 kA/cm^2 (see the supplementary material).

A. Number of transverse lasing modes

We measure the number of transverse lasing modes in cavities of different g. The laser emission passes through a diffuser and creates a speckle pattern in the far field. The number of transverse lasing modes M_l is estimated to be $1/C^2$, where C is the speckle intensity contrast.[21,29,30] Because the edge emission from the laser contains multiple transverse modes in the horizontal direction and a single guided mode in the vertical direction (perpendicular to the wafer), a line diffuser (RPC Photonics, EDL-20) is used and the far-field speckle intensity variation in the horizontal direction is recorded, as shown in Fig. 2(a).

The speckle intensity contrast C decreases with decreasing g, indicating an increase in the number of transverse lasing modes M_l. For $g = 1$, the number of transverse lasing modes, averaged over multiple devices, is ~100. Once g is reduced slightly to 0.88, M_l is enhanced 5 times to about 500. Such a rapid increase in M_l is consistent with the numerical simulation in Fig. 1(e). Further reducing $g = 0.74$ does not increase M_l any more, in contrast to the numerical results in Fig. 1(e). We attribute this difference to the spatially inhomogeneous current injection in our devices, which modifies the number of transverse lasing modes M_l (see the supplementary material). With spatially homogeneous pumping, we expect M_l to be higher, particularly for $g = 0.74$. We also note that the number of transverse lasing modes in the near-planar cavities is close to the previously reported value for a near-concentric ($g = -0.74$) cavity.[21] Therefore, even minimal curvature of the end

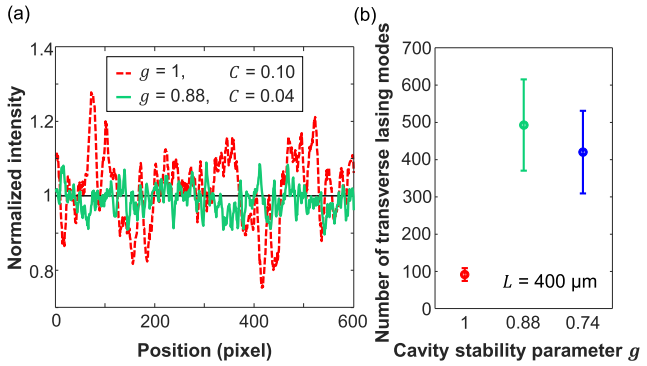

FIG. 2. Number of transverse lasing modes in near-planar cavities. (a) Measured intensity fluctuations of far-field speckles created by a line diffuser illuminated with laser emission from planar (red dashed) and near-planar (green solid) cavities. The speckle contrast C is reduced from 0.1 at $g = 1$ to 0.04 at $g = 0.88$. (b) Number of transverse lasing modes M_l, estimated from C, at two times of the lasing threshold. All laser cavities have length $L = 400$ μm (20 times longer than the simulated cavities in Fig. 1). M_l increases sharply as g decreases from 1. The error bars denote variations among multiple fabricated devices of the same geometry g.

facets is sufficient to obtain a large number of transverse lasing modes and reduce the spatial coherence.

B. Divergence of far-field emission

As more transverse modes lase, the divergence angle of the total emission increases. We measure the far-field emission pattern $I(\theta)$ in the horizontal direction, as shown in Fig. 3. The filaments in a planar cavity of $g = 1$ make $I(\theta)$ asymmetric and irregular [Fig. 3(a)]. The divergence angle $\Delta\theta$ is estimated by the full-width at half-maximum of the smoothed distribution of $I(\theta)$, and it equals 12°. With curved end facets, $\Delta\theta$ increases to 29° for $g = 0.88$ [Fig. 3(b)] and further to 39° for $g = 0.74$ [Fig. 3(c)]. We note that the measured far-field emission patterns are narrower than the simulated ones due to spatial inhomogeneity of current injection (see the supplementary material). While the increase in the lateral divergence angle in the near-planar cavities [Fig. 3(d)] is expected, the emission directionality is significantly improved compared to the near-concentric cavity[21] with $g = -0.74$ and $\Delta\theta = 70°$. Moreover, the lateral divergence of emission from the near-planar cavity is comparable to the vertical divergence of the edge emitting laser. Therefore, the output beam is approximately circular and, thus, compatible with standard collection optics.

IV. SPATIOTEMPORAL DYNAMICS

Next, we investigate the lasing dynamics of near-planar cavities and compare to the planar cavity. The emission intensity on one facet of the cavity is imaged by a ×20 objective lens onto the entrance slit of a streak camera (Hamamatsu C5680 with a fast sweep unit M5676). A single streak image covers a time window of 10 ns with a temporal resolution of about 30 ps. Figure 4(a) shows exemplary spatiotemporal intensity fluctuations of the laser emission from a planar cavity of $g = 1$. Such fluctuations comprise three different processes: (i) spatial filaments and their pulsations, (ii) spatiotemporal interference of transverse and longitudinal lasing modes, and (iii)

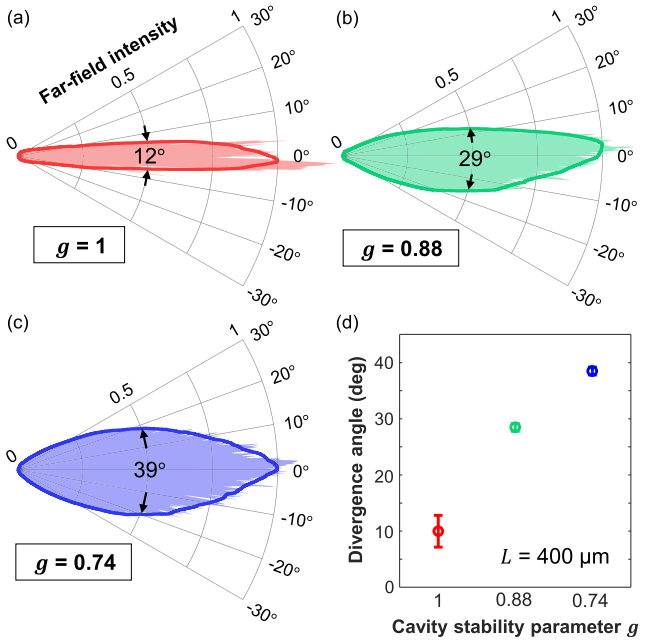

FIG. 3. Emission directionality of near-planar cavity lasers. (a)–(c) Measured far-field emission patterns $I(\theta)$ from cavities of (a) $g = 1$, (b) 0.88, and (c) 0.74. The shaded area represents the measured intensity profile, and the solid line denotes the smoothed profile with the maximal value normalized to 1. The angular full-width at half maximum $\Delta\theta$ is indicated by arrows. (d) Divergence angles $\Delta\theta$ as a function of g. All cavities have the same dimensions as those in Fig. 2. The error bars denote variations among different cavities with the same g.

photo-detection noise of the streak camera. To separate the three fluctuation processes, we resort to the fact that they feature distinct spatial and temporal scales.

A. Separation of different fluctuations

After normalizing the measured intensity $I(x,t)$ by the average $\langle I(x,t)\rangle_{x,t}$, we conduct the singular value decomposition (SVD) of the intensity fluctuation $\delta I(x,t) = I(x,t) - \langle I(x,t)\rangle_t$,

$$\delta I(x,t) = \sum_\alpha s_\alpha u_\alpha(x) v_\alpha(t), \tag{1}$$

where s_α are singular values, $u_\alpha(x)$ and $v_\alpha(t)$ are the spatial and temporal singular vectors, respectively, and α denotes the index. The singular values s_α are arranged from high to low, and they represent the contributions of the α-th singular vector to the intensity fluctuation $\delta I(x,t)$. As shown in Fig. 4(b), s_α first drops sharply with increasing α, then decays more slowly for $\alpha > 20$. Hence, the first few singular vectors with large singular values dominate $\delta I(x,t)$.

To distinguish the singular vectors, we analyze their characteristic spatial and temporal scales. The correlation functions of $u_\alpha(x)$ and $v_\alpha(t)$ are defined as

$$\begin{aligned} C_\alpha(\Delta x) &= \langle u_\alpha(x) u_\alpha(x+\Delta x)\rangle_x, \\ C_\alpha(\Delta t) &= \langle v_\alpha(t) v_\alpha(t+\Delta t)\rangle_t. \end{aligned} \tag{2}$$

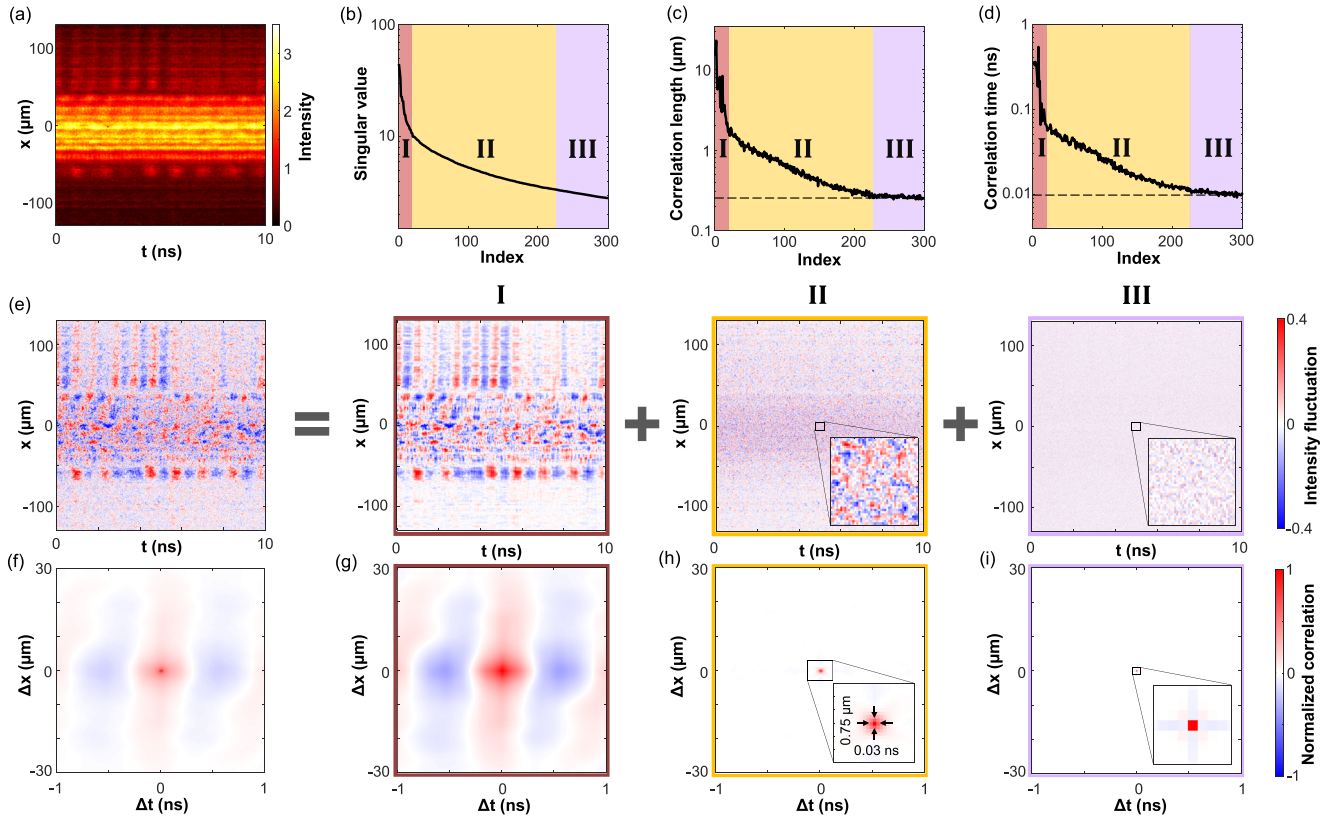

FIG. 4. Separating spatiotemporal intensity fluctuations of different origin by singular value decomposition (SVD). (a) Streak image of emission intensity $I(x,t)$ on one facet of a Fabry–Perot cavity ($g = 1$). The pump current is two times the lasing threshold. (b) Singular values obtained by SVD of intensity fluctuations $\delta I(x,t) = I(x,t) - \langle I(x,t)\rangle_t$. (c) Correlation lengths and (d) correlation times of singular vectors. The horizontal dashed lines denote the size of a single pixel in space and time of the streak image. The singular vectors are categorized into three groups I, II, and III, which are marked by red, yellow, and purple, respectively. (e) $\delta I(x,t)$ is the sum of intensity fluctuations caused by (I) filaments, (II) mode beating, and (III) detection noise. (f) The spatiotemporal correlation function of $\delta I(x,t)$ features both short- and long-range correlations. (g)–(i) Spatiotemporal correlation functions of intensity fluctuation for (g) group I, (h) II, and (i) III, exhibiting distinct correlation scales in space and time. Insets: close-up around the origin. The numbers in (h) are the spatial and temporal correlation widths.

The correlation length l_α is extracted from the full-width at half-maximum of $C_\alpha(\Delta x)$, and the correlation time τ_α from $C_\alpha(\Delta t)$. As shown in Figs. 4(c) and 4(d), both l_α and τ_α decrease rapidly with increasing α, until α reaches 20. Then, they switch to a more gradual decay and eventually level off. When α exceeds 220, both spatial and temporal correlation scales are equal to the single pixel size of the streak image.

Since s_α, l_α, and τ_α exhibit similar dependency on α, we separate the singular vectors into three groups, denoted as I, II, and III in Figs. 4(b)–4(d). Then, the spatiotemporal intensity fluctuation of each group is reconstructed by

$$\delta I_{\mathrm{R}}(x,t) = \sum_{\alpha\in\mathrm{R}} s_\alpha u_\alpha(x) v_\alpha(t), \tag{3}$$

where R is one of the three groups I, II, and III. The total intensity fluctuation is $\delta I(x,t) = \delta I_{\mathrm{I}}(x,t) + \delta I_{\mathrm{II}}(x,t) + \delta I_{\mathrm{III}}(x,t)$. In Fig. 4(e), $\delta I_{\mathrm{I}}(x,t)$, $\delta I_{\mathrm{II}}(x,t)$, and $\delta I_{\mathrm{III}}(x,t)$ display different spatial and temporal scales. To quantify the difference, we compute the spatiotemporal correlation function for each group,

$$C_{\mathrm{R}}(\Delta x,\Delta t) = \langle \delta I_{\mathrm{R}}(x,t)\delta I_{\mathrm{R}}(x+\Delta x,t+\Delta t)\rangle_{x,t}. \tag{4}$$

The spatial and temporal widths of $C_{\mathrm{R}}(\Delta x,\Delta t)$ give the correlation lengths and times for every group.

The first group $\delta I_{\mathrm{I}}(x,t)$ features strong intensity fluctuations on length scales from several to tens of micrometers, and a time scale of the order of 0.1 ns. Such scales are consistent with the typical size of spatial filaments and their oscillation frequencies. $C_{\mathrm{I}}(\Delta x,\Delta t)$ in Fig. 4(g) reveals long-range spatiotemporal correlations as a result of filament motion and pulsation.

The second group $\delta I_{\mathrm{II}}(x,t)$ features fluctuations on much shorter spatial and temporal scales. As shown in Fig. 4(e), $\delta I_{\mathrm{II}}(x,t)$ is stronger in the middle of the cavity (around $x = 0$), where the original emission intensity $I(x,t)$ in Fig. 4(a) is stronger. It implies that group II also originates from the laser emission, more precisely, from the spatiotemporal interference of all lasing modes. $C_{\mathrm{II}}(\Delta x,\Delta t)$ in Fig. 4(h) exhibits only local correlations of the intensity fluctuations.

Both the correlation length of 0.75 μm and the correlation time of 0.03 ns are limited by the resolution of our photodetection.

For the third group, $\delta I_{\mathrm{III}}(x,t)$ is uniformly spread over the entire range of the streak image. It indicates that the fluctuation is not due to the laser emission, but from the noise generated by the imaging apparatus. This is confirmed by $C_{\mathrm{III}}(\Delta x, \Delta t)$ in Fig. 4(i), which shows the spatiotemporal correlation scales equal to the pixel size of the image. Therefore, $\delta I_{\mathrm{III}}(x,t)$ represents the detection noise that fluctuates on the scale of a single pixel.

B. Spatiotemporal instabilities

The SVD can efficiently separate intensity fluctuations of different scales and origins. In Fig. 4, the three groups contain singular vectors with consecutive indices α. In general, the singular vectors in each group have similar correlation scales, but not necessarily adjacent indices. In the following text, we present a systematic way to group the singular vectors based on their correlation scales.

We acquire an ensemble of spatiotemporal intensity distributions from the same laser cavity. Within a 2 μs-long current pulse, we take 161 consecutive streak images, each covering a 10 ns window. The transient regime at the beginning of the current pulse is excluded. We perform the SVD on every streak image and compute the correlation length l_α and time τ_α for each singular vector. A scatter plot of l_α and τ_α for all singular vectors in all streak images is presented in Fig. 5(a). The black line denotes the average of correlation times for a given correlation length. Its slope changes suddenly at the correlation time of 0.07 ns, which is consistent with the boundary between groups I and II in Fig. 4(d). Moreover, the singular vectors with correlation times longer than 0.07 ns exhibit a large

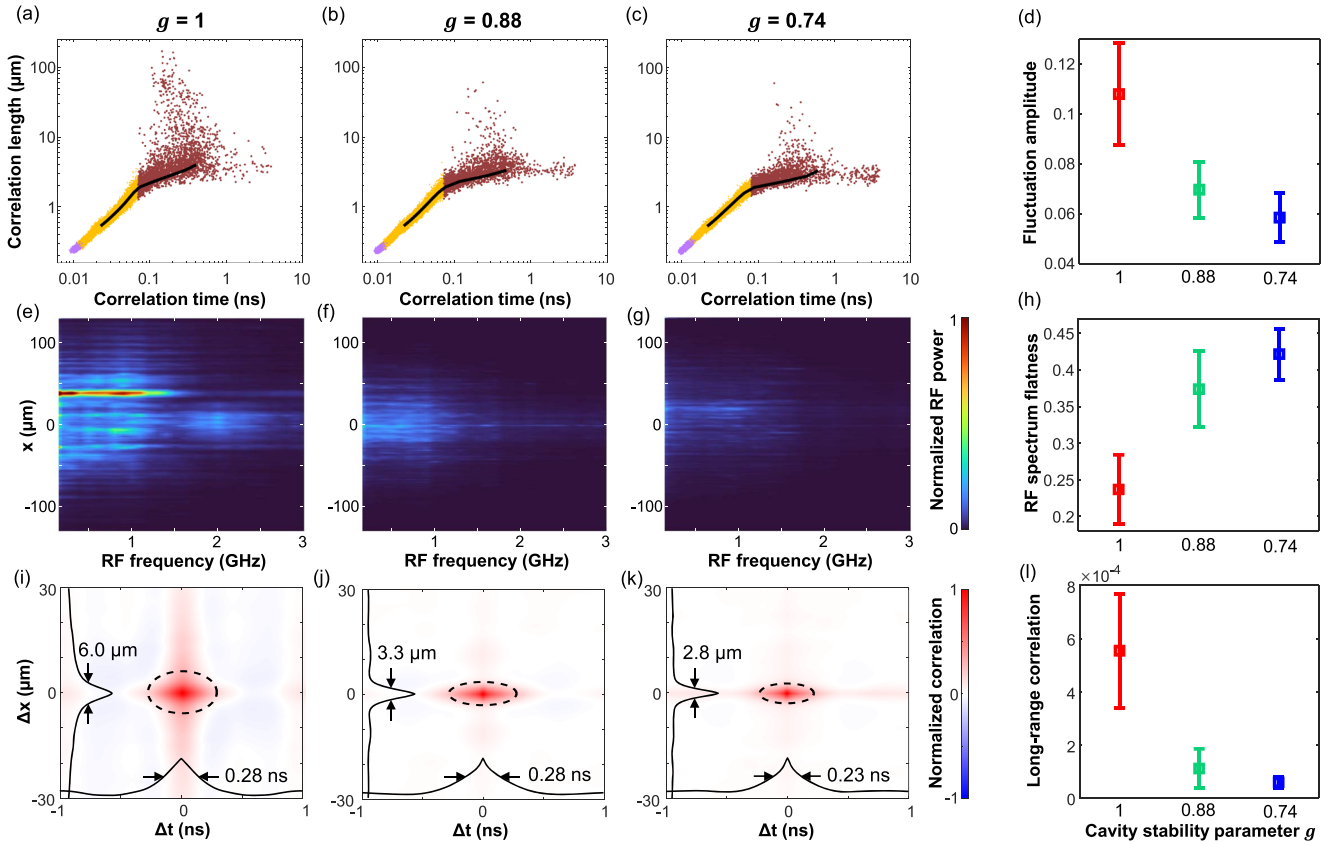

FIG. 5. Spatiotemporal dynamics of near-planar cavity lasers. (a)–(c) Scatter plots of correlation lengths and times for all singular vectors of intensity fluctuations in laser cavities with (a) $g = 1$, (b) 0.88, and (c) 0.74. The black line denotes the average correlation time at a fixed correlation length, and its slope changes suddenly at the correlation time of 0.07 ns. The three groups of singular vectors with different origin are marked by (I) red, (II) yellow, and (III) purple, respectively. (d) The amplitude of spatiotemporal intensity fluctuations caused by filaments (group I). The error bars denote variations among 5 fabricated cavities of the same g. (e)–(g) Spatially resolved radio-frequency (RF) spectra for (e) $g = 1$, (f) 0.88, and (g) 0.74, showing a clear reduction in oscillatory power as g decreases. (h) Flatness of the spatially-averaged RF spectrum for group I. The increase in flatness indicates the suppression of RF peaks corresponding to intensity oscillations. (i)–(k) Spatiotemporal correlation functions of the intensity fluctuations for group I, $C_I(\Delta x, \Delta t)$, in laser cavities of (i) $g = 1$, (j) 0.88, and (k) 0.74. The black solid lines are $C_I(\Delta x, 0)$ and $C_I(0, \Delta t)$. Their widths give the correlation length and time. The ellipse (black dashed line) divides the regions of local and nonlocal correlations, and its semi-axes are equal to the correlation length and time. (l) Long-range spatiotemporal correlations in (i)–(k), given by the averaged magnitude of the correlation outside the ellipse.

variation of the correlation length. Therefore, they belong to group I that originates from the filaments. For each time window, we sum all singular vectors with $\tau_\alpha > 0.07$ ns of a single streak image to reconstruct $\delta I_I(x,t)$ (see the supplementary material).

C. Relative intensity fluctuation

Using the same method, we investigate the spatiotemporal lasing dynamics in the near-planar cavities. Figures 5(b) and 5(c) are the scatter plots of spatial and temporal correlation scales for $g = 0.88$ and 0.74. Compared to $g = 1$ [Fig. 5(a)], the singular vectors with correlation lengths exceeding 10 μm are notably fewer, indicating that slight curving of the end facets leads to a reduction in filamentation.

For a quantitative comparison, we introduce a measure of the spatiotemporal instability. It can be shown that the square of a singular value is proportional to the fluctuation power of the corresponding singular vector (see the supplementary material). Thus, the root-mean square of the singular values s_α in group I for all time windows yields a measure for the strength of spatiotemporal instabilities, which is called the fluctuation amplitude p.

Figure 5(d) compares p for different cavity shapes. We average over 5 fabricated lasers for each g, and the error bars reflect the device-to-device variation. The mean fluctuation amplitude p for $g = 0.74$ is about half of that for $g = 1$. Therefore, the spatiotemporal dynamics becomes much more stable in the near-planar cavity lasers.

D. RF spectrum

Next, we perform the Fourier transform of $\delta I_I(x,t)$ to obtain the spatially-resolved radio-frequency (RF) spectrum for group I,

$$P(x,f) = \langle |\mathcal{F}\{\delta I_I(x,t)\}|^2 \rangle, \tag{5}$$

where $\mathcal{F}$ denotes the temporal Fourier transform and $\langle\cdot\rangle$ represents the average over different time windows. With the normalization $\langle I(x,t)\rangle_{x,t} = 1$, it is possible to compare the RF power from different cavities. In Fig. 5(e), $P(x,f)$ for $g = 1$ displays strong oscillations at a few GHz. Such oscillations become much weaker for $g = 0.88$ and 0.74 in Figs. 5(f) and 5(g).

Suppression of intensity oscillations implies that the RF spectrum has fewer features. To quantify the shape of the RF spectrum, we calculate the spectral flatness from the ratio between the geometric mean and the arithmetic mean of the power spectrum (see the supplementary material). Figure 5(h) shows the flatness of RF spectra integrated spatially and averaged over five cavities for each g. Its value increases by a factor of 2 in the near-planar cavities, confirming the suppression of temporal intensity oscillations of the laser emission.

E. Spatiotemporal correlations

Finally, we compare the spatiotemporal correlations of the laser emission intensity for different cavity shapes. Figures 5(i)–5(k) show the spatiotemporal intensity correlation functions for group I, averaged over different time windows.

The peak at the origin $\Delta x = \Delta t = 0$ is related to short-range correlations. Its full-width at half-maximum gives the correlation length, which reflects the average size of filaments. In the planar cavity [Fig. 5(i)], the correlation length is about 6 μm, and it is halved in near-planar cavities [Figs. 5(j) and 5(k)]. Thus, the filaments become narrower when the end facets are curved. The correlation time (the temporal width of the correlation function) barely changes with the cavity geometry, as it is mostly determined by the response time of the gain material (see the supplementary material).

As the filaments move around in space and time, they induce nonlocal spatiotemporal correlations in the emission intensity.[5,19,31] To quantify the long-range correlations, we average the magnitude of spatiotemporal correlations beyond the peak at the origin (see the supplementary material). Figure 5(l) shows that the long-range spatiotemporal correlations are significantly reduced for $g = 0.88$ and 0.74 compared to $g = 1$. The suppression of non-local correlations indicates that the filaments are overall weaker in the near-planar cavity lasers, thus their spatiotemporal dynamics is more stable than that of the planar-cavity laser.

V. DISCUSSION AND CONCLUSION

We demonstrate that the broad-area semiconductor laser characteristics can be dramatically changed by a small variation in the cavity shape. This is because the Fabry–Perot cavity with planar mirrors is located at a bifurcation point between stable and unstable ray dynamics. We curve the mirrors slightly and form a near-planar cavity with concave mirrors. As a result, the high-order transverse modes are well confined in the cavity, leading to a vast increase in the number of transverse lasing modes. The spatial coherence of laser emission is greatly reduced, which suppresses the speckle noise. Although the output beam has increased lateral divergence, its angular width is below 40°. Since the lateral divergence is comparable to the vertical divergence of an edge-emitting laser, the nearly circular beam can be easily collected with standard optics. Therefore, such a laser may be used as an illumination source for full-field speckle-free imaging. The advantage of our laser compared to, e.g., an incandescent lamp, which also produces no speckle noise, is that the lamp emits into far too many spatial modes and, thus, has a low power per mode, whereas our laser emits into fewer modes and, thus, features a higher power per mode and better directionality. The greatly improved brightness facilitates high-speed imaging through absorbing or scattering media and real-time monitoring of moving objects or transient processes. In fact, the decrease in spatial coherence will increase the focal spot size and reduce the intensity for optical pumping, material processing, and other applications. However, in these applications, not only the brightness, but also the beam profile matters; for example, the material processing usually requires a flat-top beam, which cannot be created by tight focusing of a spatially coherent beam. On the other hand, a laser with reduced spatial coherence may directly output a flat-top beam.[26]

Curving the end facets also leads to a drastic modification of the spatiotemporal dynamics of broad-area semiconductor lasers. With many high-order transverse modes lasing, the characteristic length scales of intensity variations in the transverse direction are greatly reduced. Consequently, the self-focusing instability induced by spatial hole burning that leads to filamentation is prevented, and the spatiotemporal instability is mitigated. For a quantitative analysis of the lasing dynamics, we develop a method to separate the intensity fluctuations caused by different processes—filaments, mode beating,

and detection noise. They have distinct spatiotemporal correlation scales, enabling us to separate filamentation from other processes. Compared to the planar cavity laser, the amplitude of spatiotemporal intensity fluctuations in the near-planar cavity is reduced by half. The RF spectrum (up to 10 GHz) becomes flattened as the temporal pulsation of the emission intensity is weakened. Finally, the reduction in filamentation in the near-planar cavity lasers decreases the long-range spatiotemporal correlations of intensity fluctuations. The stabilized laser output with negligible long-range spatiotemporal correlation will be useful for parallel random number generation.[19]

To conclude, our method efficiently controls the nonlinear lasing dynamics by tailoring the resonator shape in the vicinity of a bifurcation point. The dramatic change in the spatial structures of cavity modes strongly affects their nonlinear interactions with the gain material. Our method is simple, robust, and works for a wide range of pump currents. It may be applied to high-power fiber and solid-state lasers, as well as other nonlinear dynamical systems. It can also be employed to control the time-reversed lasing and coherent perfect absorption.[32–35]

SUPPLEMENTARY MATERIAL

See the supplementary material for additional details of the experiment and numerical simulations.

ACKNOWLEDGMENTS

The authors acknowledge the computational resources provided by the Yale High Performance Computing Cluster (Yale HPC). H.C. acknowledges support from the Office of Naval Research under Grant No. N00014-221-1-2026. S.B. acknowledges support for the Chair in Photonics from the Ministère de l'Enseignement Supérieur, de la Recherche et de l'Innovation, Région Grand-Est, Département Moselle, European Regional Development Fund (ERDF), Metz Métropole, GDI Simulation, CentraleSupélec, and Fondation CentraleSupélec. Q. J. Wang acknowledges support from Singapore A*STAR funding A18A7b0058, and Singapore National Research Foundation funding NRF-CRP19-2017-01 and NRF-CRP23-2019-0007. O.H. acknowledges support from the Science Foundation Ireland (SFI) via Grant No. 18/RP/6236.

AUTHOR DECLARATIONS

Conflict of Interest

The authors have no conflicts to disclose.

DATA AVAILABILITY

The data that support the findings of this study are available within the article and its supplementary material.

REFERENCES

[1] A. E. Siegman, "New developments in laser resonators," in *Optical Resonators* (International Society for Optics and Photonics, 1990), Vol. 1224, pp. 2–14.
[2] H. Kogelnik and T. Li, "Laser beams and resonators," Appl. Opt. **5**, 1550–1567 (1966).
[3] A. E. Siegman, *Lasers* (University Science Books, 1986).
[4] N. Hodgson and H. Weber, *Laser Resonators and Beam Propagation: Fundamentals, Advanced Concepts, Applications* (Springer, 2005), Vol. 108.
[5] I. Fischer, O. Hess, W. Elsäßer, and E. Göbel, "Complex spatio-temporal dynamics in the near-field of a broad-area semiconductor laser," Europhys. Lett. **35**, 579 (1996).
[6] O. Hess, "Spatio-temporal complexity in multi-stripe and broad-area semiconductor lasers," Chaos, Solitons Fractals **4**, 1597–1618 (1994).
[7] O. Hess and T. Kuhn, "Maxwell–Bloch equations for spatially inhomogeneous semiconductor lasers. II. Spatiotemporal dynamics," Phys. Rev. A **54**, 3360 (1996).
[8] J. R. Marciante and G. P. Agrawal, "Spatio-temporal characteristics of filamentation in broad-area semiconductor lasers," IEEE J. Quantum Electron. **33**, 1174–1179 (1997).
[9] J. R. Marciante and G. P. Agrawal, "Spatio-temporal characteristics of filamentation in broad-area semiconductor lasers: Experimental results," IEEE Photonics Technol. Lett. **10**, 54–56 (1998).
[10] D. Scholz, H. Braun, U. T. Schwarz, S. Brüninghoff, D. Queren, A. Lell, and U. Strauss, "Measurement and simulation of filamentation in (Al, In) GaN laser diodes," Opt. Express **16**, 6846–6859 (2008).
[11] M. Arahata and A. Uchida, "Inphase and antiphase dynamics of spatially-resolved light intensities emitted by a chaotic broad-area semiconductor laser," IEEE J. Sel. Top. Quantum Electron. **21**, 522–530 (2015).
[12] J. Salzman, R. Lang, S. Margalit, and A. Yariv, "Tilted-mirror semiconductor lasers," Appl. Phys. Lett. **47**, 9–11 (1985).
[13] R. Lang, J. Salzman, and A. Yariv, "Modal analysis of semiconductor lasers with nonplanar mirrors," IEEE J. Quantum Electron. **22**, 463–470 (1986).
[14] J. Salzman, T. Venkatesan, R. Lang, M. Mittelstein, and A. Yariv, "Unstable resonator cavity semiconductor lasers," Appl. Phys. Lett. **46**, 218–220 (1985).
[15] J. Salzman, R. Lang, A. Larson, and A. Yariv, "Confocal unstable-resonator semiconductor laser," Opt. Lett. **11**, 507–509 (1986).
[16] M. L. Tilton, G. C. Dente, A. H. Paxton, J. Cser, R. K. Defreez, C. E. Moeller, and D. Depatie, "High power, nearly diffraction-limited output from a semiconductor laser with an unstable resonator," IEEE J. Quantum Electron. **27**, 2098–2108 (1991).
[17] S. A. Biellak, C. G. Fanning, Y. Sun, S. S. Wong, and A. E. Siegman, "Reactive-ion-etched diffraction-limited unstable resonator semiconductor lasers," IEEE J. Quantum Electron. **33**, 219–230 (1997).
[18] H. Adachihara, O. Hess, E. Abraham, P. Ru, and J. V. Moloney, "Spatiotemporal chaos in broad-area semiconductor lasers," J. Opt. Soc. Am. B **10**, 658–665 (1993).
[19] K. Kim, S. Bittner, Y. Zeng, S. Guazzotti, O. Hess, Q. J. Wang, and H. Cao, "Massively parallel ultrafast random bit generation with a chip-scale laser," Science **371**, 948–952 (2021).
[20] S. A. Biellak, Y. Sun, S. S. Wong, and A. E. Siegman, "Lateral mode behavior of reactive-ion-etched stable-resonator semiconductor lasers," J. Appl. Phys. **78**, 4294–4296 (1995).
[21] K. Kim, S. Bittner, Y. Zeng, S. F. Liew, Q. Wang, and H. Cao, "Electrically pumped semiconductor laser with low spatial coherence and directional emission," Appl. Phys. Lett. **115**, 071101 (2019).
[22] L. Li, "The advances and characteristics of high-power diode laser materials processing," Opt. Lasers Eng. **34**, 231–253 (2000).
[23] K. Shigihara, Y. Nagai, S. Karakida, A. Takami, Y. Kokubo, H. Matsubara, and S. Kakimoto, "High-power operation of broad-area laser diodes with GaAs and AlGaAs single quantum wells for Nd:YAG laser pumping," IEEE J. Quantum Electron. **27**, 1537–1543 (1991).
[24] A. Müller, S. Marschall, O. B. Jensen, J. Fricke, H. Wenzel, B. Sumpf, and P. E. Andersen, "Diode laser based light sources for biomedical applications," Laser Photonics Rev. **7**, 605–627 (2013).
[25] B. Redding, M. A. Choma, and H. Cao, "Speckle-free laser imaging using random laser illumination," Nat. Photonics **6**, 355–359 (2012).
[26] H. Cao, R. Chriki, S. Bittner, A. A. Friesem, and N. Davidson, "Complex lasers with controllable coherence," Nat. Rev. Phys. **1**, 156–168 (2019).
[27] S. Bittner, S. Guazzotti, Y. Zeng, X. Hu, H. Yılmaz, K. Kim, S. S. Oh, Q. J. Wang, O. Hess, and H. Cao, "Suppressing spatiotemporal lasing instabilities with wave-chaotic microcavities," Science **361**, 1225–1231 (2018).
[28] L. Ge, Y. D. Chong, and A. D. Stone, "Steady-state ab initio laser theory: Generalizations and analytic results," Phys. Rev. A **82**, 063824 (2010).

[29] J. W. Goodman, *Speckle Phenomena in Optics: Theory and Applications* (Roberts and Company Publishers, 2007).
[30] B. Redding, A. Cerjan, X. Huang, M. L. Lee, A. D. Stone, M. A. Choma, and H. Cao, "Low spatial coherence electrically pumped semiconductor laser for speckle-free full-field imaging," Proc. Natl. Acad. Sci. U. S. A. **112**, 1304–1309 (2015).
[31] O. Hess and T. Kuhn, "Spatio-temporal dynamics of semiconductor lasers: Theory, modelling and analysis," Prog. Quantum Electron. **20**, 85–179 (1996).
[32] Y. D. Chong, L. Ge, H. Cao, and A. D. Stone, "Coherent perfect absorbers: Time-reversed lasers," Phys. Rev. Lett. **105**, 053901 (2010).
[33] A. Ghobadi, H. Hajian, B. Butun, and E. Ozbay, "Strong light–matter interaction in lithography-free planar metamaterial perfect absorbers," ACS Photonics **5**, 4203–4221 (2018).
[34] G. Liu, J. Chen, P. Pan, and Z. Liu, "Hybrid metal-semiconductor meta-surface based photo-electronic perfect absorber," IEEE J. Sel. Top. Quantum Electron. **25**, 1–7 (2018).
[35] P. Tang, G. Liu, X. Liu, G. Fu, Z. Liu, and J. Wang, "Plasmonic wavy surface for ultrathin semiconductor black absorbers," Opt. Express **28**, 27764–27773 (2020).